Geomechanics and Engineering, *Vol. 39, No. 4 (2024) 385-396*
https://doi.org/10.12989/gae.2024.39.4.385

Landslide mapping using a combination of sentinel-2 multi spectral instruments and GIS data at Namwon, Jeollabuk-do, South Korea

Hwan-Hui Lim[1], Seung-Min Lee[2], Enok Cheon[1], Eu Song[3], Jun-Seo Jeon[4] and Seung-Rae Lee*[1]

[1]*Water Infrastructure Research Center, K-water Research Institute, Daejeon 34141, Republic of Korea*
[2]*The 21st Infantry Division of the Republic of Korea Armed Forces, Yang-gu, Korea*
[3]*Landslide Team, Department of Forest Environment and Conservation, National Institute of Forest Science, Seoul 02455, Republic of Korea*
[4]*Department of Geotechnical Engineering Research, Korea Institute of Civil Engineering and Building Technology, Goyang-si 10223, Republic of Korea*

(*Received March 5, 2024, Revised October 16, 2024, Accepted November 11, 2024*)

Abstract. With the recent development of satellite, aerial, and remote sensing technologies, it is easy to produce landslide inventory maps over a large area. In this study, the object-based framework was designed to address the limitations inherent in the pixel-based deep learning (DL) methodology. This framework explores the potential of combining Sentinel-2 MultiSpectral Instrument (MSI) satellite imagery and digital elevation models (DEMs) to enhance shallow landslide mapping across diverse terrains comprehensively. The study area for analysis and verification was selected as Jucheon-myeon, Namwon-si, and Jeollabuk-do, where significant large-scale landslides and slope failures occurred in 2020. As a result, the application of this framework led to the classification of 68 candidate sites spanning an area of 0.5 hectares or more. Site surveying was conducted on 20 random sites with a 1ha or more scale. Furthermore, six sites were selected where satellite imagery could discern the damaged areas. At these locations, the damaged area estimated by the framework was compared with the actual observed damaged area to assess accuracy. These rapid and cost-effective landslide mapping techniques can accurately estimate the location and extent of landslides and enhance the precision of sensitivity models and land management strategies.

Keywords: image classification; inventory map; landslide; object-based image analysis; satellite

1. Introduction

Landslides are commonly occurring natural disasters worldwide, and landslides with high speeds, large scales, and strong impact forces can have significant economic impacts and potentially cause extensive damage to social infrastructure like roads and buildings (Jakob *et al.* 2005). In Korea, 63% of the land area is mountainous terrain, and areas with thin soil layers are highly susceptible to landslides (Park *et al.* 2016). Furthermore, the central region of Korea receives over 50% of its annual precipitation from July to September, making this area prone to landslides during this season (Lee *et al.* 2021). As a result, human, material, and economic damage continues to occur, and the damage caused by landslides over the past 30 years is shown in Fig. 1.

Consequently, investigating and understanding this significant natural threat, along with offering susceptibility modeling and mapping, is essential for the prevention and reduction of its devastating impacts (Hua *et al.* 2021, Nanehkaran *et al.* 2021, Zhao *et al.* 2020). This approach to analysis and modeling necessitates accurate landslide inventory maps (Huang *et al.* 2020). Furthermore, the swift mapping of landslides after heavy rainfall or seismic

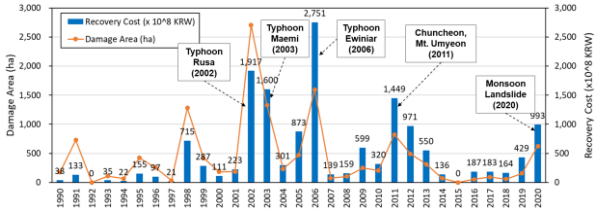

Fig. 1 Damage caused by landslides in Korea from 1976 to 2020 (Cheon 2022)

activities is crucial for timely interventions, humanitarian assistance, and various disaster relief efforts (He *et al.* 2022, Rindraharisaona *et al.* 2022, Jitt-Aer *et al.* 2022). Traditionally, landslide inventories have been generated through field surveys and/or manual interpretation of aerial photographs and satellite imagery (Guzzetti *et al.* 2012, Scaioni *et al.* 2014).

The extraction of information from satellite imagery predominantly utilizes two methodologies: pixel-based analysis and object-based image analysis (OBIA) (Kucharczyk *et al.* 2020). Pixel-based image analysis primarily focuses on comparing the spectral similarities among pixels for image classification (Zerroiki *et al*. 2014).

Spectral pattern recognition serves as a fundamental approach in land cover classification, employing the spectral data inherent to each pixel to facilitate this process (Oruc *et al*. 2004). However, the efficacy of pixel-based spectral pattern recognition methods has been challenged by

*Corresponding author, Professor
E-mail: srlee@kaist.ac.kr

ISSN: 2005-307X (Print), 2092-6219 (Online)

advancements in high-resolution remote sensing imagery. In such imagery, individual pixels correspond to ground areas ranging from 0.25 to 2 meters, significantly augmenting the complexity and heterogeneity of the objects that can be discerned (Qin *et al*. 2015). Therefore, machine learning (ML) models, including decision trees, support vector machines (SVMs), artificial neural networks (ANNs), and random forests (RF), have been utilized to mitigate these challenges (Ghiasi *et al.* 2023, Nitze *et al*. 2012, Ujjwal *et al.* 2022). However, despite the varied efficacies of these ML models, pixel-based methodologies exhibit certain limitations, particularly in the context of very high resolution (VHR) satellite imagery (Chen *et al.* 2018). The nuanced complexities within very high-resolution (VHR) images are challenging to capture with high fidelity, requiring significant time and financial investment for processing extensive data volumes. These limitations negatively impact the accuracy of both image classification and landslide detection tasks. Conversely, given the constraints of pixel-based methodologies in image processing, particularly in classification, Object-Based Image Analysis (OBIA) has gained prominence as a strategy to surmount the shortcomings inherent in pixel-level analysis, especially pertinent to high-resolution and very high-resolution remote sensing imagery (Hussain *et al.* 2013, Syed 2015). Object-based image analysis distinguishes itself from pixel-based analysis by focusing on objects formed through the aggregation of pixels, instead of analyzing individual pixels. It involves a two-step process: initially, segmentation occurs, which partitions the image into smaller, meaningful objects, followed by the classification of these segmented objects. Segmentation constitutes the foundational and crucial step in object-based classification, exerting significant influence on the outcomes of classification. The segmentation process needs to be dynamic to accommodate objects of varying sizes, hence bottom-up methods are predominantly employed. A bottom-up approach commences at the individual pixel level, aggregating it with neighboring pixels according to similarity in attributes. Multi-resolution segmentation is a common technique in this context, where the amalgamation of adjacent objects is guided by parameters like scale, as well as spectral and spatial properties (Gao *et al*. 2011). Consequently, object-based image analysis incorporates comprehensive data, including spectral features, geometric shapes, dimensions, and structural details, thereby addressing the limitations of pixel-based classifications by organizing pixels into coherent, higher-level entities (Troya-Galvis *et al.* 2015).

Furthermore, object-based methods facilitate the derivation of additional attributes such as the mean, standard deviation, and aspect ratio, enhancing the extraction of salient information like texture, contextual relationships, and spatial dynamics, alongside spectral data. This enriched analytical framework enables more precise land classification outcomes (Baatz 2000). In this study, the mapping of landslides and the estimation of damaged areas were performed using an object-based approach, augmented by a framework that synergistically combines spectral and topographic information.

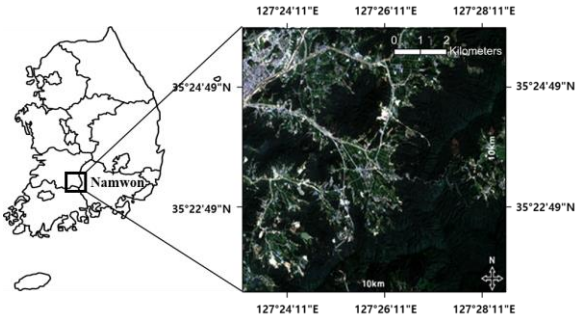

Fig. 2 Location map showing the study area

The study area selected for this research was the region surrounding Jucheon-myeon, Namwon, Jeollabuk-do, which suffered the most significant landslide damage in 2020 (Korea Forest Service. 2020). Object-based image analysis techniques were applied using high-resolution Sentinel-2 MultiSpectral Instrument (MSI) images and a digital elevation model (DEM) to identify landslide sites through satellite remote sensing. After data acquisition, the MultiSpectral images and DEM are processed through object segmentation and geographic information system (GIS) processing. The processed data are finally used to generate a landslide inventory map by classifying non-vegetation, soil, steep slopes, and long-thin objects. The overall procedure identified 68 different landslide regions in a 500 m^2 region. During the field investigation of landslides, comparative analysis and validation were conducted to assess the accuracy of the landslide site identification process and the quantification of the damaged area.

2. Study area

The study area was the region of Jucheon-myeon, Namwon, Jeollabuk-do, Korea (Fig. 2). In this area, 20 ha (1 ha = 10,000 m^2) of landslide damage was caused by heavy rainfall in July and August 2020. This site was selected since the study area needed to be an area where landslides that occurred could be identified with the naked eye considering the satellite images to be used and the resolution (10 m) of the digital elevation model. Therefore, areas that suffered the most significant landslide damage in 2020 were selected. For efficient calculation, the image area was limited to a 10 km x 10 km region, centered around the Myeon Office (the geographical center of Jucheon-myeon). According to data from the Myeon Office, the entire area of Jucheon-myeon is surrounded by large and small mountains with altitudes ranging from 200 m to 1000 m. The ground of the surrounding mountainous areas is mainly composed of granite and weathered granite soil. The Sentinel-2 satellite images acquired on August 20, 2020 were used in this study.

South Korea's climate is characterized by complex patterns due to the interplay between continental and oceanic influences, with an average annual precipitation of 1,190 mm. Over 50% of this total annual rainfall occurs during the monsoon season, which lasts from July to

September. Fig. 2 displays rainfall data from a meteorological station located 6 km away from the landslide site, as provided by the Korea Meteorological Administration (KMA). Typhoon Hagupit brought heavy rainfall to the region on August 5, 2020. The total accumulated rainfall from July 27 to August 13 amounted to 794 mm, with a significant portion of this, 430.1 mm, recorded on August 7 and 8.

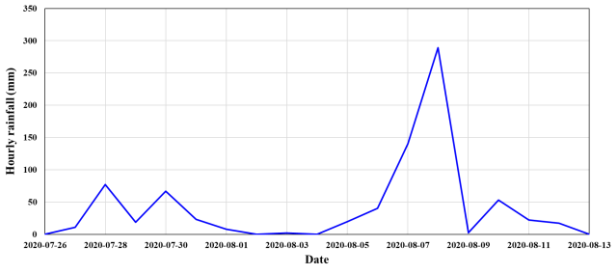

Fig. 3 Hourly rainfall (From on July 26th to August 13th)

3. Methods

3.1 Objective-based image analysis

A pixel-based image analysis is a prevalent image analysis method. However, this technique has limitations in recognizing individual pixels as actual geographical objects and does not consider relationships between neighboring pixels. As a result, texture and shape information cannot be accurately reflected, leading to lower classification accuracy. To overcome these limitations, this study employed an object-based image analysis. The OBIA differs from the pixel-based image analysis in that it operates on a group of pixels forming an object rather than individual pixels. The process of object-based image analysis involves two main steps: segmentation, where small objects are generated, and classification of the segmented images. Segmentation is a crucial step in the object-based classification, as it directly impacts the accuracy of the classification results. If object sizes need to be specified, a bottom-up method is typically used, as objects of varying sizes cannot be accurately classified. The bottom-up method begins with a single pixel and then merges it with neighboring pixels based on homogeneity criteria. Multi-resolution segmentation is commonly used with this approach, where the merging of two adjacent objects is based on spectral and spatial information as well as scale parameters (Goa *et al.* 2011). The image analysis encompasses various aspects such as spectral characteristics, geometric shape, size, and structural information. However, the object-based image analysis overcomes the limitations of pixel-based image classification by grouping pixels into higher-level objects (Andres *et al.* 2015). In addition, the object-based classification offers advantages over the pixel-based classification by enabling the derivation of characteristics such as average value, standard deviation, and length/width ratio. The object-based classification can achieve highly accurate land classification results by combining spectral information with other features, such as texture, relationships with surroundings, and spatial information (Battz *et al.* 2000).

3.2 Land slide mapping framework

As shown in Fig. 3, the developed framework for identifying landslide regions through the object-based image analysis involves the following processes: (1) satellite image and digital map acquisition, (2) pre-processing of the acquired image, (3) image object segmentation, (4) segmentation optimization, (5) classification hierarchy, and (6) accuracy assessment.

The Sentinel-2 MSI satellite images were taken on August 20, 2020, and the digital map used in the DEM was created by the National Geographic Information Institute in 2020. In order to increase the efficiency of the computational process, the pre-processing of the satellite images was limited to a square-shaped 100 km^2 area (10 km x 10 km) centered around Jucheon-myeon, Namwon, Jeollabuk-do. Among the pre-processed images, the multi-resolution segmentation was performed using four bands (Red, Green, Blue, and Near-Infrared [NIR]) of Sentinel-2 MSI with a resolution of 10 m. The four bands were used to classify non-vegetated areas and soil areas based on the normalized difference vegetation index (NDVI) and the normalized difference soil index (NDSI).

The spectral difference segmentation was performed to merge objects generated from the segmentation process with similar spectral characteristics into one object. In the segmentation process, the object size should be set to be similar to the actual size of the landslide area. Therefore, the segmentation optimization process was performed to adjust the landslide area to be consistent with actual landslides. Then, the length/width ratio was measured to classify landslide occurrence areas based on morphological characteristics. Finally, the DEM was used to compute the average slope of the object.

Verification was conducted to confirm the occurrence of landslides in areas classified as non-vegetated areas, soil areas, and steep slopes with morphological characteristics of landslides. It is generally performed by comparing very high-resolution (VHR) satellite or aerial images of a site before and after landslide events. However, since no pre-developed inventory maps or super-resolution maps of the study area were available, on-site verification was performed in this study.

3.3 Optimization of object-based image analysis

In this study, Sentinel-2 MSI satellite images and a DEM were analyzed using object-based image analysis and terrain analysis softwares. The Sentinel-2 MSI can acquire spectral data across 13 bands (Table 1). For this study, the Red, Green, Blue, and Near-infrared bands were used for the spectral analysis. Additionally, these four bands provided the highest resolution of 10 meters, providing more details than the other bands. Segmentation was performed using the four bands, and the resulting objects

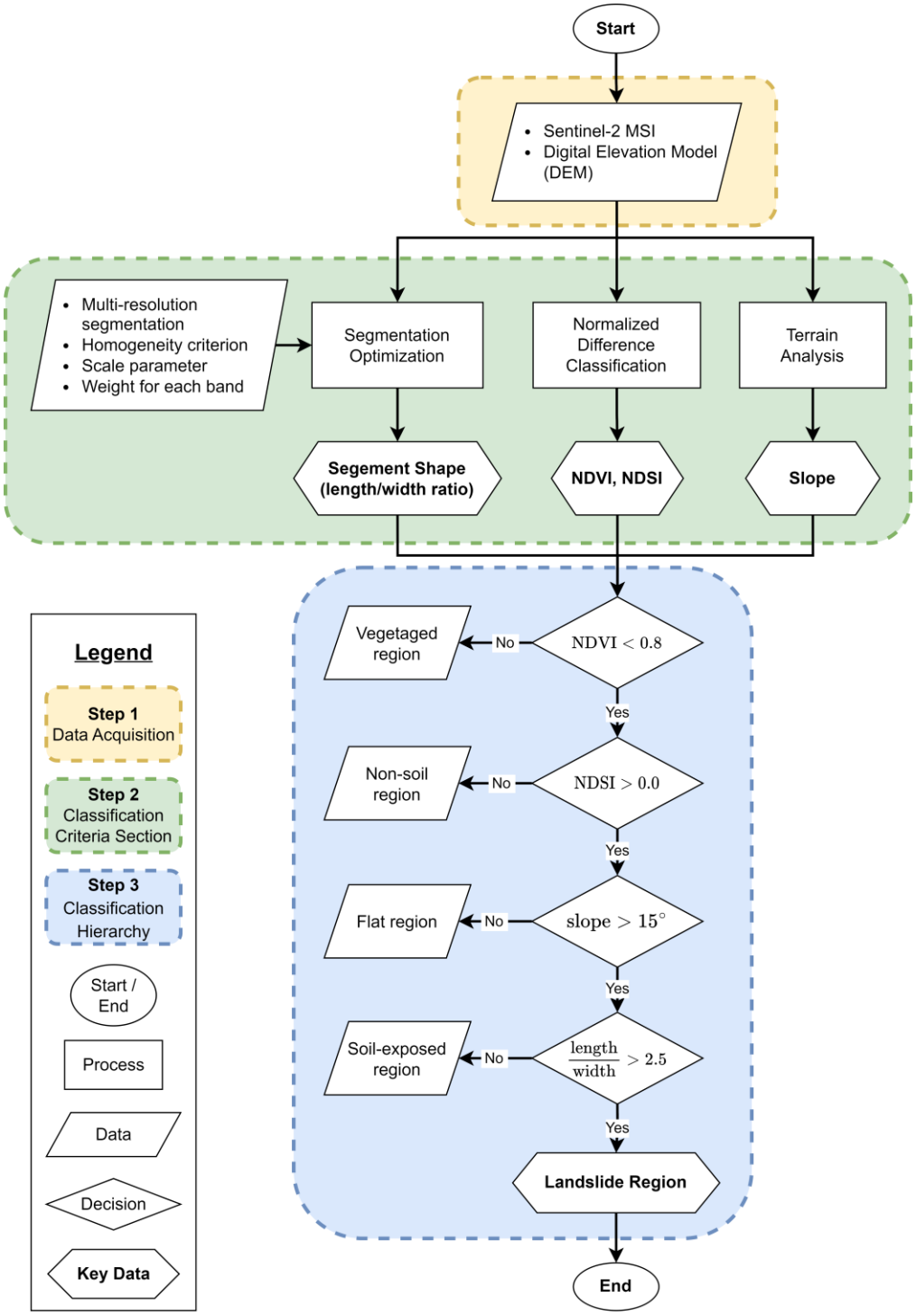

Fig. 4 Flowchart of the landslide occurrence identification process based on object-based image analysis

were subjected to a four-step classification process. The DEM used in this study was a digital map produced by the National Geographic Information Institute and has a resolution of 10 meters to be consistent with the resolution of the four bands used in the Sentinel-2 MSI image. The object-based image analysis was conducted using eCognition Developer 9.4 software developed by eCognition® (Trimble Germany GmbH, 2021), and the ArcMap 10.6.1 software (ESRI, 2018) was used for the terrain analysis.

3.3.1 Segmentation optimization

The Image segmentation is a critical initial step in the object-based image analysis. The objects generated in the segmented image are used for further segmentation or classification to facilitate the landslide analysis. It is essential to aim for an accurate depiction of objects that closely resemble reality to achieve the desired level of segmentation (Lu *et al.* 2011). Describing a landslide region as a single entity is challenging due to the complex characteristics of land, including changes in land cover,

Table 1 Unit Wavelength and Resolution by Sentinel-2 MSI Band

Band	Central wavelength (μm)	Resolution (m)
Band 1 – Coastal aerosol	0.443	60
Band 2 - Blue	0.490	10
Band 3 - Green	0.560	10
Band 4 – Red	0.665	10
Band 5 – Red Edge	0.705	20
Band 6 – Red Edge	0.740	20
Band 7 – Red Edge	0.783	20
Band 8 - NIR	0.842	10
Band 8A – Red Edge	0.865	20
Band 9 – Water vapour	0.945	60
Band 10 – SWIR - Cirrus	1.375	60
Band 11 - SWIR	1.610	20
Band 12 – SWIR	2.190	20

variations in illuminance, diverse spectral distributions, and fluctuations in size (Martha el al., 2010). To overcome this problem, the multi-resolution segmentation is utilized, enabling the creation of objects based on a specified minimum object size (Benz *et al*. 2004).

In this study, 14 object size variables (scale parameters = 10, 15, 20, 25, 30, 35, 40, 45, 50, 60, 70, 80, 90, and 100) were used to specify the minimum object size value. As shown in Fig. 5, different scale parameters result in changes in object size during the segmentation process. From the tested scale parameters, a scale parameter value of 50 was determined as the optimal value because the object sizes generated more closely matched visually to the sizes of the landslide regions and provided sufficient resolution for an efficient analysis. In addition, by specifying a weight for each spectral difference between neighboring objects, the multi-resolution segmentation further refined the segmentation objects by merging objects with similar spectra.

3.3.2 Normalization difference classification

The normalized difference vegetation index (NDVI), which is defined in (Eq. (1)), is a widely used vegetation index calculated from the difference between red and near-infrared reflectance (Tucker *et al.* 1979, Cracknell *et al.* 2001). The NDVI is strongly correlated with the degree of photosynthesis, activation of chlorophyll, and energy absorption (Castro *et al.* 1998). When applied to a plant community, this index provides a measure of the "greenness" of an area, indicating the amount, condition, or degree of vitality of vegetation in a given area. The NDVI is a dimensionless index expressed in exponential units and ranges from –1 to +1 (Meneses *et al.* 2011). The NDVI was used to remove vegetation in the study area, and the

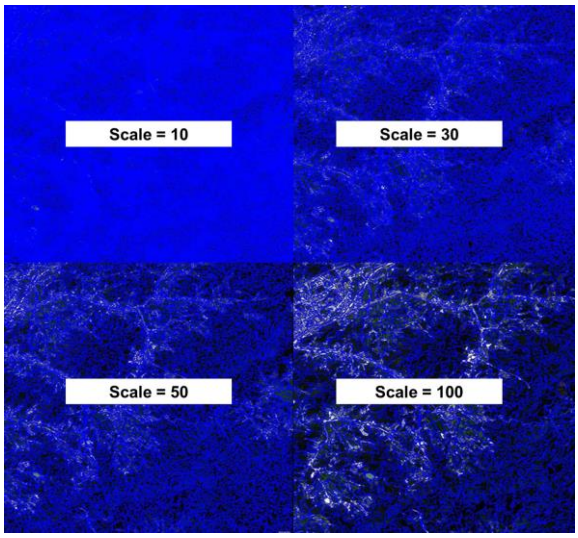

Fig. 5 Multi-resolution segmentation by optimal scale parameter (scale parameter = 10, 30, 50, 100)

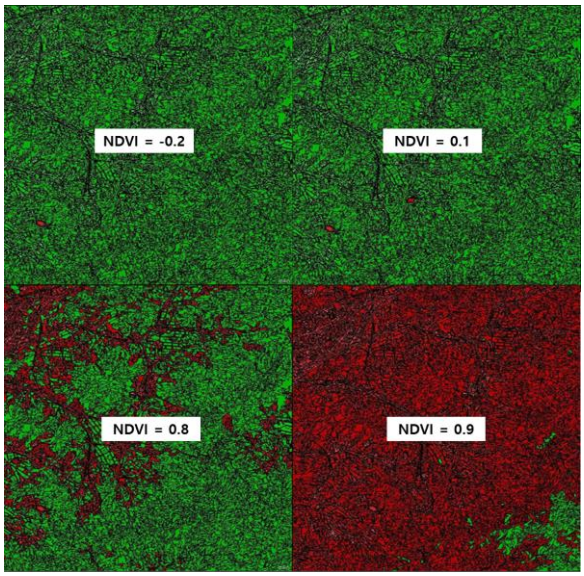

Fig. 6 Vegetation classification according to NDVI (Green = Vegetation)

normalized difference soil index (NDSI) was used to separate soil. In this study, twelve levels of values, specifically -0.2, -0.1, 0, 0.1, 0.2, 0.3, 0.4, 0.5, 0.6, 0.7, 0.8, and 0.9, were applied to determine the optimal NDVI. As a result, the optimal NDVI was set as 0.8. The NDVI value is set higher than the commonly used reference value of 0.5 to classify areas with dense vegetation considering the acquisition time of the satellite images (Fig. 6). Furthermore, setting a low threshold for the NDVI standard results in 80 to 90% of the study area being classified as vegetated. Consequently, this classification could erroneously include areas where landslides have actually occurred as vegetated regions. This approach aims to mitigate the risk of overlooking areas of actual landslide occurrence, even in scenarios where the extent of vegetated areas is underestimated, resulting in a classification that covers less area than exists in reality.

$$NDVI = \frac{Reflectance\ (NIR) - Reflectance\ (Red)}{Reflectance\ (NIR) + Reflectance\ (Red)} \quad (1)$$

where the Band strong represents a band with a relatively high value and Band weak is a band with a relatively low value. This equation involves a relatively high and relatively low reflectance within the land cover's soil. The difference between the two bands of the land cover information was normalized to distinguish it from other land cover types (Major *et al.* 1990, Gao 1996). Unlike the NDVI, the NDSI doesn't apply a uniform band selection across all regions. The primary reason is the inherent complexity of soil, which has diverse chemical and physical properties. This intricate spectrum limits establishing a straightforward linear relationship between soil attributes and their spectral response (Ben 2002). This stems from the fact that while different land cover types should exhibit unique spectral characteristics for clear distinction, soils do not consistently do so (Mahlein *et al.* 2013). Secondly, the spectral characteristics of soil vary based on its structure, texture, moisture content, color, and surface roughness (Lõhmus *et al.* 1989). For instance, soils that bear moss typically have a higher water content, leading them to exhibit spectral properties akin to those of moisture and shadow, among others (Wu *et al.* 2004). As a result, it has different values depending on the researcher's choice, the area studied, and the images used. In this study, spectral characteristics were analyzed for 60 samples (ten samples from six different locations within the study area, as shown in Tables 2 to 7).

Table 2 Digital number of the soil samples (A region – soil)

	Band 2	Band 3	Band 4	Band 8	Band 11
Site 1	918	1388	1610	3426	2985
Site 2	1354	1880	2475	3527	3637
Site 3	739	1144	1351	3007	2711
Site 4	606	745	987	2531	1856
Site 5	840	1050	1334	2590	2505
Site 6	986	1351	1664	2572	2751
Site 7	751	1137	1146	3422	2573
Site 8	604	805	943	2533	2400
Site 9	598	780	913	2450	2031
Site 10	824	1232	1422	3797	3438
AVG	747.5	1046.8	1259	2714.8	2445.3

Table 3 Digital number of the soil samples (B region – soil)

	Band 2	Band 3	Band 4	Band 8	Band 11
Site 1	533	753	896	2431	3385
Site 2	504	705	834	2409	3074
Site 3	651	861	1072	2603	3558
Site 4	914	1265	1418	3079	3327
Site 5	772	1074	1314	3427	2793
Site 6	1043	1410	1630	3208	3634
Site 7	1176	1533	1748	3201	3262
Site 8	728	1101	1045	3490	2595
Site 9	1294	1548	1964	2979	2877
Site 10	683	1068	1023	3108	2640
AVG	754.5	1029.2	1177.1	2722.1	2832.4

Table 4 Digital number of the soil samples (C region – soil)

	Band 2	Band 3	Band 4	Band 8	Band 11
Site 1	855	1056	1322	2599	2305
Site 2	705	905	1200	2728	2348
Site 3	865	1264	1627	2774	3023
Site 4	915	1391	1741	3677	3198
Site 5	1207	1621	2032	3090	3040
Site 6	1222	1542	2135	3033	3814
Site 7	1240	1639	2153	3264	3003
Site 8	739	1004	1306	2767	2978
Site 9	1149	1584	1930	3574	3147
Site 10	2302	2842	3501	4284	5170
AVG	1018.3	1350.1	1,722.8	2,890.7	2,912.5

Table 5 Digital number of the soil samples (D region – downtown)

	Band 2	Band 3	Band 4	Band 8	Band 11
Site 1	1543	1692	1749	2217	2324
Site 2	1263	1456	1544	1929	2023
Site 3	1516	1734	1809	2449	2547
Site 4	1321	1587	1576	2294	2250
Site 5	1250	1372	1377	2318	2268
Site 6	1836	2026	2142	2320	2541
Site 7	1222	1420	1482	2240	2720
Site 8	1124	1301	1403	1621	2251
Site 9	955	1117	1216	2064	2504
Site 10	1538	1703	1779	2021	1891
AVG	1,233.6	1,401.0	1,461.9	1,952.8	2,120.9

Table 6 Digital number of the soil samples (E region – mountain)

	Band 2	Band 3	Band 4	Band 8	Band 11
Site 1	256	412	224	2556	1174
Site 2	253	406	216	2436	1104
Site 3	277	428	229	2991	1280
Site 4	288	403	224	2532	1112
Site 5	273	417	229	2695	1183
Site 6	260	384	207	2456	1067
Site 7	229	337	197	1861	955
Site 8	254	384	195	2912	1374
Site 9	296	479	250	3945	1527
Site 10	262	397	218	2547	1242
AVG	240.9	368.2	199.4	2,449	1,093.5

Table 7 Digital number of the soil samples (F region – mountain)

	Band 2	Band 3	Band 4	Band 8	Band 11
Site 1	266	420	221	2977	1396
Site 2	279	423	223	2765	1182
Site 3	223	378	176	3946	1838
Site 4	263	388	223	3565	2179
Site 5	202	350	170	3678	1772
Site 6	239	342	181	2919	1501
Site 7	212	268	129	2243	1449
Site 8	241	387	174	4169	1941
Site 9	218	338	159	2879	1385
Site 10	239	354	195	2512	1203
AVG	216.7	331.9	168.6	2,878.3	1,441.5

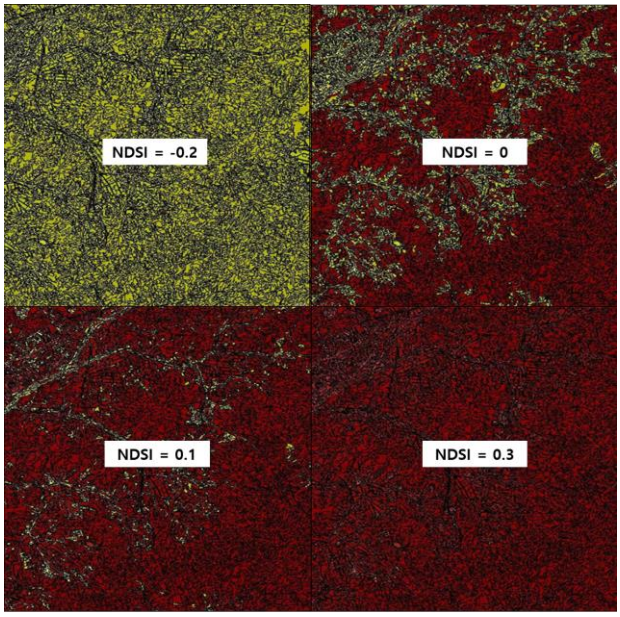

Fig. 7 Land classification according to NDSI (Yellow = Soil)

In the case of Sentinel-2 data, the relationship between Digital Number (DN) and reflectance (with reflectance being measured in its default unit) can be expressed as: $\mathrm{DN} = 10{,}000 \times \text{reflectance}$ (Sentinelhub., Sinergise Ltd). As a result, the reflectance in Band 4 (Red) was relatively higher than the reflectance in Band 2 (Blue) and was consistent. Therefore, the Band that can represent soil when applying the normalized difference index to the study area can be expressed as the relational expression between Bands 2 and 4, as described in (Eq. (3)). The proposed equation was utilized to classify the soil within the study area as a NDSI (Fig. 7). Similar to NDVI, the NDSI also necessitates the selection of a reference value. To determine the optimal Normalized Difference Snow Index (NDSI), a comprehensive application of twelve distinct values was conducted, namely: -0.2, -0.1, -0.075, -0.05, -0.025, 0, 0.025, 0.05, 0.075, 0.1, 0.2, and 0.3. Consequently, similar to the classification of vegetation areas, a relatively low

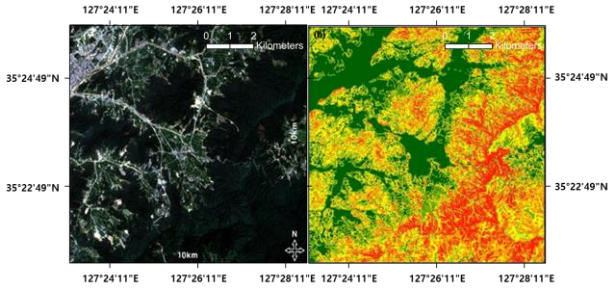

Fig. 8 Slope classification of study area

threshold of 0.0 was employed to identify as many potential landslide sites as possible.

$$SITE\ NDSI = \frac{Reflectance\ (Band\ 4) - Reflectance\ (Band\ 2)}{Reflectance\ (Band\ 4) + Reflectance\ (Band\ 2)} \quad (3)$$

3.3.3 Slope and length/width ratio

Satellite imagery was employed to differentiate between non-vegetated and soil-covered areas, while a DEM facilitated the classification of steep and flat terrains. The classification of slopes using the DEM was conducted with ArcMap 10.6.1 software. A slope of 15° was set to distinguish steep slopes from flat regions because the frequency of landslides rapidly decreases when the slope is less than 15° (Barlow *et al.* 2006, Ahsen *et al*. 2020). Fig. 4 displays the slope classification results, with areas having a slope greater than 15 degrees highlighted in orange.

After identifying potential landslide sites with NDVI, NDSI, and slope, the geometry of each object was used as an additional filter for classifying landslides. Besides being non-vegetated land, soil land, and steep slopes, the landslide zones are generally long and thin. Therefore, the length-to-width ratio of the objects was used as a landslide criterion. An empirical examination of the aerial photograph inventory showed that the ratio of landslide movement length to width was greater than 2.5 (Barlow *et al*. 2006, Martha *et al*. 2010). Consequently, by applying the length-to-width ratio standard within the developed framework to classify areas as non-vegetated, soil, and steep terrain, we identified 68 objects each with an area of 500 m² or more, as illustrated in Fig. 8.

4. Results and discussion

4.1 Landslide site classification

The object-based image analysis was performed for the study area. Using Sentinel-2 MSI satellite images and a DEM, landslide candidate areas were classified using the developed framework.

As previously shown, the segmentation optimization process used the scale parameter value of 50. The objects generated using the optimal scale parameter were similar in size to the actual landslides. In the classification hierarchy, landslide candidate areas are classified using NDVI, NDSI, slope, and object geometry. Firstly, the NDVI standard was set as 0.8, and areas above the standard were classified as

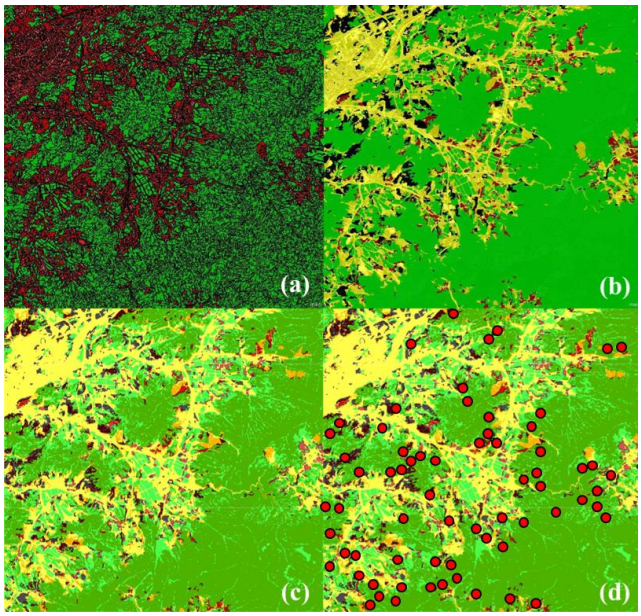

Fig. 9 Landslide site classification results: (a) NDVI classification, (b) NDVI, NDSI classification, (c) NDVI, NDSI, slope classification and (d) NDVI, NDSI, slope, length/width classification (68 sites)

vegetation (Fig. 9(a)). Subsequently, an NDSI criterion of 0.0 was applied to classify soil areas (Fig. 9(b)), and steep slope areas were classified by setting the critical slope value as 15° (Fig. 9(c)). Finally, areas with a length-to-width ratio of 2.5 or higher were classified as landslide sites (Fig. 9(d)). As a result, 68 objects in the study area with a minimum area of 500 m^2 were classified as candidate areas. Then, on-site verification was performed by randomly selecting 20 areas with an area of 1,000 m^2or more.

4.2 Field verification landslide map and accuracy assessment

Various methods are employed to verify the accuracy of landslide inventory maps, the most common examples being comparisons with existing maps, analysis of ultra-high-definition aerial or satellite images, and on-site verifications. However, no inventory maps or high-quality images of the study area selected for this research were available for comparison. Therefore, on-site verification was the primary method used for accuracy assessment. Among the 68 classified locations, 20 candidate areas with areas of 1,000 m^2 or more were randomly selected (Fig. 10). Following the on-site inspections at the 20 chosen locations, clear indications of landslides were observed in 17 of these areas, as shown in Fig. 9. Conversely, the remaining three locations exhibited no signs of landslides; however, they were identified as steep slopes with a heightened risk of such events occurring. Therefore, based on the field verification results, the developed framework with object-based images has proven to be able to accurately generate landslide inventory maps for the selected study area.

Table 8 Comparison of landslide area

	Area (m^2)	
	Site investigation	OBIA Framework
Site 1	4.75×10^4	5.05×10^4
Site 2	1.5×10^4	1.85×10^4
Site 3	20×10^4	20.45×10^4
Site 4	2.17×10^4	2.25×10^4
Site 5	6.73×10^4	6.95×10^4
Site 6	2×10^4	2.35×10^4

4.3 Estimation of landslide occurrence area

To assess the accuracy of the estimated landslide damage area using the developed OBIA-based framework, the six sites exhibiting the most significant landslide damage among the 20 selected were chosen for comparison against the actual observed landslide damage areas (Fig. 11). The survey of the landslide damage area was carried out at the National Institute of Forest Science between July 21 and August 11, 2020. Table 8 presents a comparison between the actual landslide areas and those estimated by the OBIA framework. The relative error rate was utilized to evaluate accuracy. The findings indicated that the discrepancy between the estimated landslide damage area via the OBIA-based framework and the actual landslide damage area was approximately 9.39%. This suggests that the framework can provide an accurate prediction of the landslide damage area when implemented in field settings. Notably, the framework demonstrates greater accuracy in regions with extensive damage compared to those with minimal damage. Consequently, it is suitable for application in mapping regions prone to high landslide risks and in assessing large-scale landslide damage areas.

5. Conclusions

This study developed an object-based image analysis (OBIA) framework designed to improve the accuracy of landslide mapping by utilizing Sentinel-2 MSI satellite imagery and digital elevation models (DEM). By integrating geospatial and spectral parameters such as the normalized difference vegetation index (NDVI), the normalized difference soil index (NDSI), slope, and object geometry (length-to-width ratio), we successfully applied the framework to Jucheon-myeon, Namwon-si, Jeollabuk-do, a region that experienced significant landslide damage in 2020. The framework identified 68 landslide-prone areas, characterized as non-vegetated, steep, soil-covered, and elongated in shape. Among these areas, 20 larger sites were selected for field verification, and on-site inspections confirmed landslide traces at 17 of these locations, with the remaining three identified as steep slopes with a heightened risk of landslides. The developed framework achieved a relative error rate of approximately 9.39% when comparing the estimated landslide damage area to the actual observed damage, demonstrating the framework's effectiveness in real-world applications.

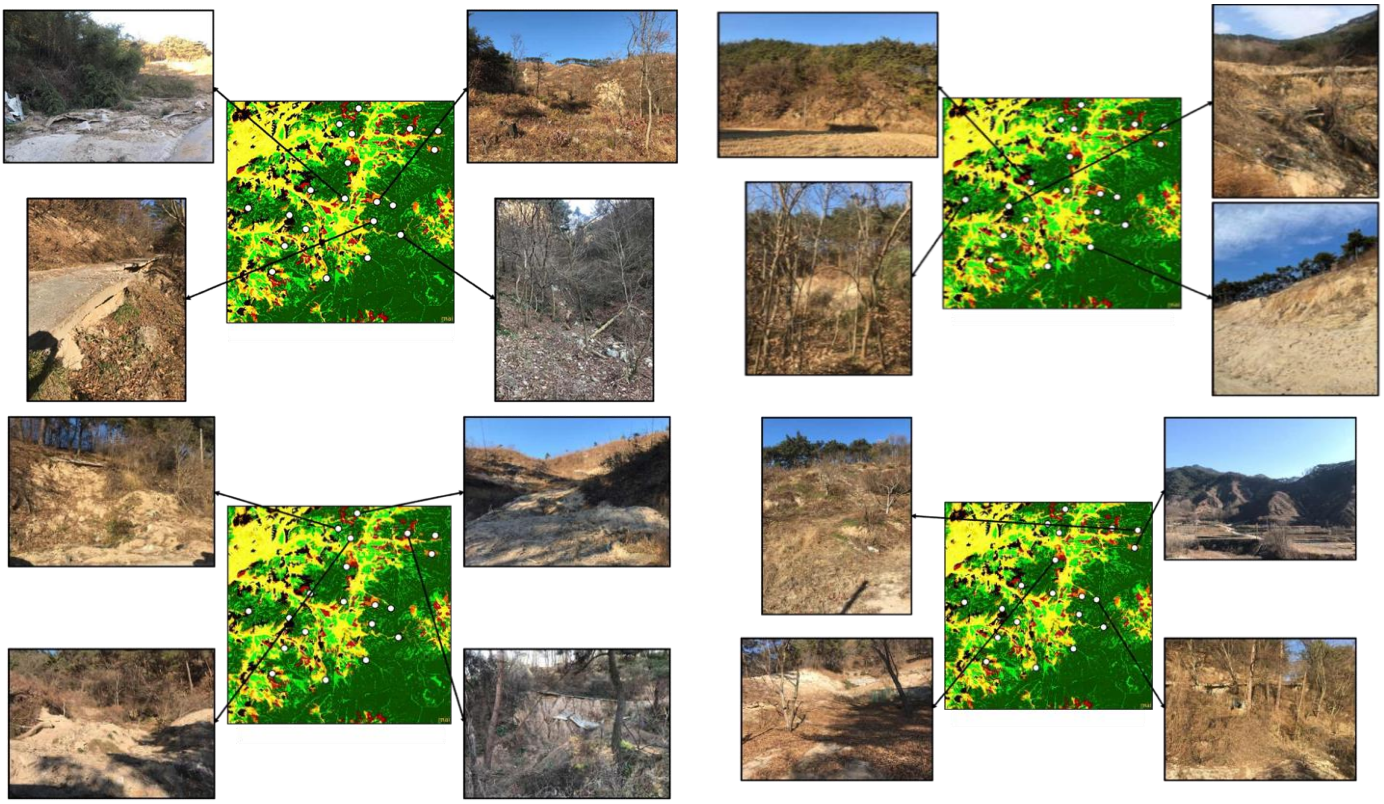

Fig. 10 Site verification of landslide sites (20 sites)

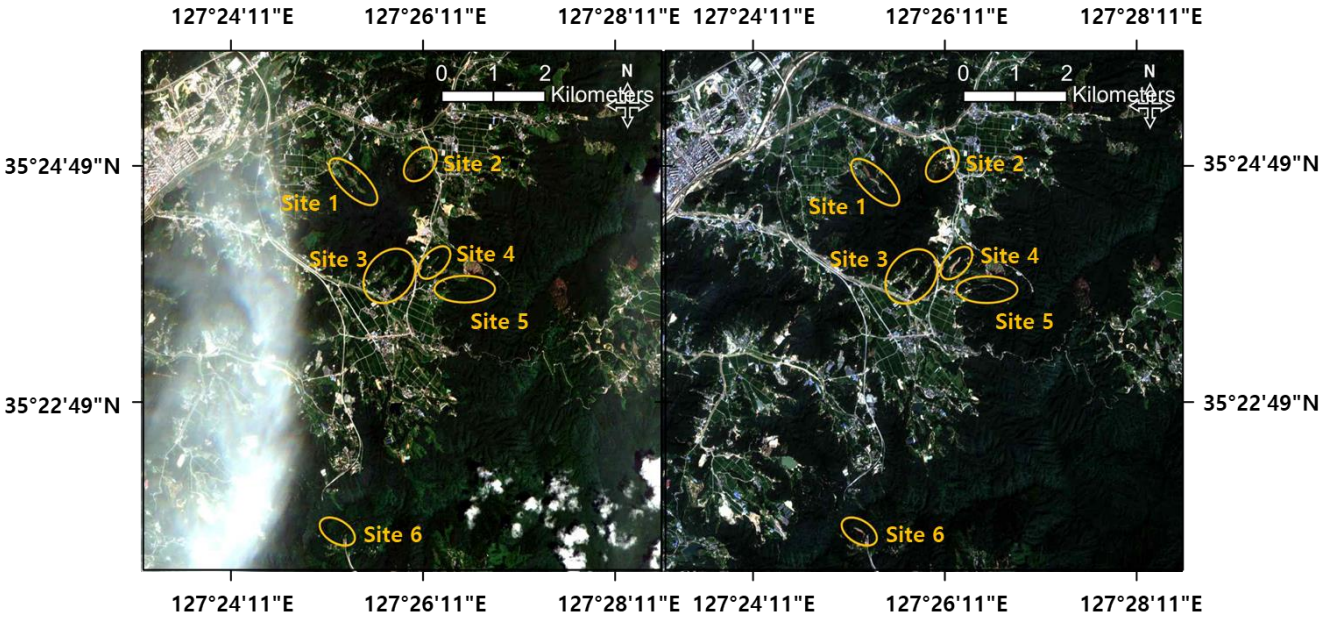

Fig. 11 Pre- and post-landslide imagery comparison in the study area (Pre : July 21, 2020, Pro : August 20, 2020)

Despite these promising results, it is important to acknowledge a key limitation of this study: the use of data from 2020. Although the data were suitable for verifying the framework's accuracy at that time, landslide conditions in the study area may have evolved since then. Landslide-affected areas are dynamic and can change significantly due to ongoing natural processes, human intervention, and environmental factors such as climate change. Consequently, future studies should incorporate more recent satellite imagery and updated environmental data to better reflect current landslide occurrence conditions. Applying this framework to recent data would further validate its applicability and improve the accuracy of future landslide assessments.

Nevertheless, the framework developed in this study demonstrates considerable potential for broad application. Its flexibility allows for adaptation to different types of landslides and diverse geographic areas. With additional refinement, such as the inclusion of updated environmental variables, this framework could be extended beyond its original scope to monitor and classify various types of slope failures, including debris flows and rockslides. Conducting further research on the soil composition and geological characteristics of landslide-prone regions would also enhance the framework's ability to differentiate between landslide types, improving both precision and specificity in landslide mapping.

Moreover, integrating machine learning techniques into the OBIA framework represents an exciting avenue for future research. Machine learning could facilitate the automation of landslide detection and classification, making it possible to process and analyze larger datasets more efficiently. This would enable real-time or near-real-time landslide monitoring, which is crucial for timely disaster response, particularly in regions highly susceptible to landslides. By automating the framework, large-scale applications—such as regional or national landslide inventory mapping—could be undertaken with reduced human intervention, significantly improving the speed and efficiency of landslide risk assessments.

Ultimately, this study presents an innovative and scalable solution for landslide mapping that goes beyond traditional pixel-based approaches. By combining high-resolution satellite imagery, geospatial analysis, and object-based classification methods, the framework offers a more precise and comprehensive means of identifying landslide-prone areas. While this study focused on data from 2020, the developed framework holds significant promise for future research and practical applications. By incorporating more recent data and integrating machine learning techniques, the framework could be refined into a powerful tool for ongoing disaster management and mitigation efforts. Future studies will continue to expand and refine the framework, ensuring that it remains a valuable asset in landslide detection, risk assessment, and disaster response in an increasingly dynamic and unpredictable world.

Acknowledgments

This paper was supported by the Ministry of Land, Infrastructure and Transport of the Korean government (Project No.: RS-2020-KA157130) and Korea Electric Power Corporation (Grant number: R22XO05-05).

References

Amatya, P., Kirschbaum, D. and Stanley, T. (2019), "Use of very high-resolution optical data for landslide mapping and susceptibility analysis along the Karnali highway", *Remote Sens.*, **11,** 2284. https://doi.org/10.3390/rs11192284.

Amatya, P., Kirschbaum, D., Stanley, T. and Tanyas, H. (2021), "Landslide mapping using object-based image analysis and open source tools", *Eng. Geol.*, **282**, 106000. https://doi.org/10.1016/j.enggeo.2021.106000.

Baatz, M. and Schäpe, A. (2000), "Multiresolution segmentation— an optimization approach for high quality multi-scale image segmentationl", *Agewandte Geoinfomatik Symposium.*, 12-23.

Barlow, J., Franklin, S. and Martin, Y. (2006), "High spatial resolution satellite imagery, DEM derivatives, and image segmentation for the detection of mass wasting processes", *Photogramm. Eng. Rem. S.*, **6**, 687-692. https://doi.org/10.14358/PERS.72.6.687.

Ben-Dor, E. (2002), "Quantitative remote sensing of soil properties. 173-243".

Benz, Ursula C., Peter, H., Gregor, W., Iris, L., Markus, H. (2004), "Multi-resolution, object-oriented fuzzy analysis of remote sensing data for GIS-ready information", *ISPRS J. Photogramm. Rem. S.*, **58**(3-4), 239-258. https://doi.org/10.1016/j.isprsjprs.2003.10.002.

Castro, R. and Chuvieco, E. (1998), "Modeling forest fire danger from geographic information systems", *Geocarto Int.*, **13**(1), 15-23. https://doi.org/10.1080/10106049809354624.

Comert, R., Avdan, U., Gorum, T. and Nefeslioglu, H.A. (2019), "Mapping of shallow landslides with object-based image analysis from unmanned aerial vehicle data", *Eng. Geol.*, **260**, 105264. https://doi.org/10.1016/j.enggeo.2019.105264.

Cracknell, A.P.. (2001), "The exciting and totally unanticipated success of the AVHRR in applications for which it was never intended", *Adv. Sp. Res.*, **28**(1), 233-240. https://doi.org/10.1016/S0273-1177(01)00349-0.

Deng, Y., Wu, C., Li, M. and Chen, R. (2015), "RNDSI: A ratio normalized difference soil index for remote sensing of urban/suburban environments", *Int. J. Appl. Earth Observ. Geoinformation*, **39**, 40-48. https://doi.org/10.1016/j.jag.2015.02.010.

Gao, B.C. (1996), "NDWI—A normalized difference water index for remote sensing of vegetation liquid water from space", *Remote Sens. Environ.*, **58**(3), : 257-266. https://doi.org/10.1016/S0034-4257(96)00067-3.

Gao, Y.A.N., Mas, J.F., Kerle, N. and Navarrete Pacheco, J.A. (2011), "Optimal region growing segmentation and its effect on classification accuracy", *Int. J. Remote Sens.*, **32**(13), 3747-3763. https://doi.org/10.1080/01431161003777189

Ghiasi, V., Pauzi, N.I.M., Karimi, S. and Yousefi, M. (2023), "Landslide risk zoning using support vector machine algorithm", *Geomech. Eng.*, **34**(3), 267, https://doi.org/10.12989/gae.2023.34.3.267.

Goa, Y.A.N., Mas, J.F. and Navarrete Pacheco, J.A. (2011), "Optimal region growing Segmentation And Its Effect on Classification Accuracyl", *Int. J. Remote Sens.*, **32**(13), 3747-3763. https://doi.org/10.1080/01431161003777189.

Guzzetti, F., Mondini, A.C., Cardinali, M., Fiorucci, F., Santangelo, M. and Chang, K.T. (2012), "Landslide inventory maps: new tools for an old problem", *Earth Sci. Rev.*, **112**, 42-66. https://doi.org/10.1016/j.earscirev.2012.02.001.

He, K., Ma, G., Hu, X., Liu, B. and Han, M. (2022), "The July 2, 2017, Lantian landslide in Leibo, China: mechanisms and mitigation measures", *Geomech. Eng.*, **28**(3), 283-298. https://doi.org/10.12989/gae.2022.28.3.283

Holbling, D., Abad, L., Dabiri, Z., Prasicek, G., Tsai, T.T. and Argentin, A.L. (2020), "Mapping and analyzing the evolution of the Butangbunasi landslide using landsat time series with respect to heavy rainfall events during typhoons", *Appl. Sci.*, **10**, 630. https://doi.org/10.3390/app10020630.

Hua, Y., Wang, X., Li, Y., Xu, P. and Xia, W. (2021), "Dynamic development of landslide susceptibility based on slope unit and deep neural networks", *Landslides*, **18**, 281-302. https://doi.org/10.1007/s10346-020-01444-0.

Huang, F., Zhang, J., Zhou, C., Wang, Y., Huang, J. and Zhu, L.

(2020), "A deep learning algorithm using a fully connected sparse autoencoder neural network for landslide susceptibility prediction", *Landslides*, **17**, 217-229. https://doi.org/10.1007/s10346-019-01274-9.

Hussain, M., Chen, D., Cheng, A., Wei, H. and Stanley, D. (2013), "Change detection from remotely sensed images: From pixel-based to object-based approaches", *ISPRS J. Photogramm. Rem. S.*, **80**, 91-106. https://doi.org/10.1016/j.isprsjprs.2013.03.006.

Jakob, M., Hungr, O. and Jakob, D.M. (2005), *Debris-flow hazards and related phenomena*.

Jitt-Aer, K., Wall, G., Jones, D. and Teeuw, R. (2022), "Use of GIS and dasymetric mapping for estimating tsunami-affected population to facilitate humanitarian relief logistics: a case study from Phuket, Thailand", *Nat. Hazards*, **113**(1), 185-211.

Keyport, R.N., Oommen, T., Martha, T.R., Sajinkumar, K.S. and Gierke, J.S. (2018), "A comparative analysis of pixel-and object-based detection of landslides from very high-resolution images", *Int. J. Appl. Earth Obs. Geoinf.*, **64**, 1-11. https://doi.org/10.1016/j.jag.2017.08.015.

Korea Forest Service. (2020), *Landslide damage status*. http://sansatai.forest.go.kr/gis/main.do;jsessionid=JZOrYq15hn0d19d74MGj7yGHjYXvAP1oYh2NcaUiC81TqDXOVaN19nppMaMcVfXM.ext-fdiswas1_servlet_ldm#mhms7. Accessed August 31 2020.

Kucharczyk, M., Hay, G.J., Ghaffarian, S. and Hugenholtz, C.H. (2020), "Geographic object-based image analysis: a primer and future directions", *Remote Sens.*, **12**(12), 2012. https://doi.org/10.3390/rs12122012.

Lee., D.H., Cheon, E., Lim, H.H., Choi, S.K., Kim, Y.T. and Lee, S.R. (2021), "An artificial neural network model to predict debris-flow volumes caused by extreme rainfall in the central region of South Korea", *Eng. Geol.*, **281**, 105979. https://doi.org/10.1016/j.enggeo.2020.105979.

Liu, L.L., Yang, C. and Wang, X.M. (2021), "Landslide susceptibility assessment using feature selection-based machine learning models", *Geomech. Eng.*, **25**(1), 1-16. https://doi.org/10.12989/gae.2021.25.1.001.

Lõhmus, K., Oja, T. and Lasn, R. (1989), "Specific root area: a soil characteristic", *Plant Soil*, **119**, 245-249.

Lu, P., Stumpf, A., Kerle, N., and Casagli, N. (2011), "Object-oriented change detection for landslide rapid mapping", *IEEE Geosci. Remote Sens. Lett.*, **8**(4), 701-705. https://doi.org/10.1109/LGRS.2010.2101045.

Mahlein, A.K., Rumpf, T., Welke, P., Dehne, H.W., Plümer, L., Steiner, U. and Oerke, E.C. (2013), "Development of spectral indices for detecting and identifying plant diseases", *Remote Sens. Environ.*, **128**, 21-30. https://doi.org/10.1016/j.rse.2012.09.019.

Major, D.J., Baret, F. and Guyot, G. (1990), "A ratio vegetation index adjusted for soil brightness", *Int. J. Remote Sens.*, **11**(5), 727-740. https://doi.org/10.1080/01431169008955053.

Maqsoom, A., Aslam, B., Khalil, U., Kazmi, Z.A., Azam, S. Mehmood, T. and Nawaz, A. (2022), "Landslide susceptibility mapping along the China Pakistan Economic Corridor (CPEC) route using multi-criteria decision-making method", *Model. Earth Syst. Environ.*, **8**, 1519-1533.

Martha, T.R., Kerle, N., Jetten, V., van Westen, C.J. and Kumar, K.V. (2010), "Characterising spectral, spatial and morphometric properties of landslides for semi-automatic detection using object-oriented methods", *Geomorphology*, **116**(1-2), 24-36. https://doi.org/10.1016/j.geomorph.2009.10.004.

Meneses-Tovar, C.L. (2011), "NDVI as indicator of degradation", Unasylva.

Moosavi, V., Talebi, A. and Shirmohammadi, B. (2014), "Producing a landslide inventory map using pixel-based and object-oriented approaches optimized by Taguchi method", *Geomorphology*, **204**, 646-656. https://doi.org/10.1016/j.geomorph.2013.09.012.

Nanehkaran, Y.A., Mao, Y., Azarafza, M., Kockar, M.K. and Zhu, H.H. (2021), "Fuzzy-based multiple decision method for landslide susceptibility and hazard assessment: A case study of Tabriz, Iran", *Geomech. Eng.*, **24**(5), 407-418. https://doi.org/10.12989/gae.2021.24.5.407.

Nitze, I., Schulthess, U. and Asche, H. (2012), "Comparison of machine learning algorithms random forest, artificial neural network and support vector machine to maximum likelihood for supervised crop type classification", *Proceedings of the 4th GEOBIA*, Rio de Janeiro, Brazil.

Oruc, M., Marangoz, A.M. and Buyuksalih, G. (2004), "Comparison of pixel-based and object-oriented classification approaches using Landsat-7 ETM spectral bands", İstanbul, Turkyie.

Park, D.W., Vasu, N.N., Lee, S.R., Kang, S.H. and Park, J.Y. (2016), "Coupled model for simulation of landslides and debris flows at local scale", *Nat. Hazards*, **81**(3), 1653-1682.

Qin, R., Huang, X., Gruen, A. and Schmitt, G. (2015), "Object-based 3-D building change detection on multitemporal stereo images", *IEEE J. Select. Topics Appl. Earth Observ. Remote Sens.*, **8**(5), 2125-2137. https://doi.org/10.1109/JSTARS.2015.2424275.

Rindraharisaona, E.J., Réchou, A., Fontaine, F.R., Barruol, G., Stamenoff, P., Boudevillain, B. and Delcher, E. (2022), "Seismic signature of rain and wind inferred from seismic data", *Earth Sp. Sci.*, 9(10), e2022EA002328. https://doi.org/10.1029/2022EA002328.

Scaioni, M., Longoni, L., Melillo, V. and Papini, M. (2014), "Remote sensing for landslide investigations: an overview of recent achievements and perspectives", *Remote Sens.*, **6**(10), 9600-9652. https://doi.org/10.3390/rs6109600.

Sentinel Hub, Sinergise Ltd., https://www.sentinel-hub.com.

Sur, U., Singh, P., Meena, S.R. and Singh, T.N. (2022), "Predicting landslides susceptible zones in the Lesser Himalayas by ensemble of per pixel and object-based models", *Remote Sens.*, **14**(8), 1953. https://doi.org/10.3390/rs14081953.

Syed, A.H. (2015), "Segmentation and Classification of Remotely Sensed Images: Object-based image analysis", Rochester Institute of Technology.

Trimble Germany GmbH (2021), "Trimble Documentation eCognition Developer 10.1 Reference Book", Trimble Germany GmbH: Munich, Germany.

Troya-Galvis, A., Gancarski, P., Passat, N. and Berti-Equille, L. (2005), "Unsupervised quantification of under-and over-segmentation for object-based remote sensing image analysis", *IEEE J. Select. Topics Appl. Earth Observ. Remote Sens.*, **8**(5) : 1936-1945. https://doi.org/10.1109/JSTARS.2015.2424457.

Troya-Galvis, A., Gançarski, P., Passat, N. and Berti-Equille, L. (2015), "Unsupervised quantification of under-and over-segmentation for object-based remote sensing image analysis", *IEEE J. Select. Topics Appl. Earth Observ. Remote Sens.*, **8**(5), 1936-1945. https://doi.org/10.1109/JSTARS.2015.24244573.

Tucker, C.J. (1979), "Red and photographic infrared linear combinations for monitoring vegetation", *Remote Sens. Environ.*, **8**(2), 127-150. https://doi.org/10.1016/0034-4257(79)90013-0.

Wu, C. (2004), "Normalized spectral mixture analysis for monitoring urban composition using ETM+ imagery", *Remote Sens. Environ.*, **93**(4), : 480-492. https://doi.org/10.1016/j.rse.2004.08.003.

Zerrouki, N. and Bouchaffra, D. (2014, October), "Pixel-based or object-based: Which approach is more appropriate for remote sensing image classification", *Proceedings of the 2014 IEEE International Conference on Systems, Man, and Cybernetics (SMC)*, IEEE.

Zhao, L., Huang, Y., Xiong, M. and Ye, G. (2020), "Reliability

and risk assessment for rainfall-induced slope failure in spatially variable soils", *Geomech. Eng.*, **22**(3), 207-217. https://doi.org/10.12989/gae.2020.22.3.207.

GC